Interaction of Mixed-Ligand Mono layer-Protected Au-144 Clusters with Biomimetic Membranes as a Function of the Transmembrane Potential

4 AUTHORS, INCLUDING:

Lucia Becucci
University of Florence
72 PUBLICATIONS   **1,376** CITATIONS

SEE PROFILE

Rolando Guidelli
University of Florence
226 PUBLICATIONS   **3,889** CITATIONS

SEE PROFILE

Federico Polo
University of Padova
16 PUBLICATIONS   **430** CITATIONS

SEE PROFILE

Interaction of Mixed-Ligand Monolayer-Protected Au$_{144}$ Clusters with Biomimetic Membranes as a Function of the Transmembrane Potential

Lucia Becucci,*,[†] Rolando Guidelli,[†] Federico Polo,[‡] and Flavio Maran*,[‡]

[†]Department of Chemistry, Florence University, via della Lastruccia 3, 50019 Sesto Fiorentino (Firenze), Italy

[‡]Department of Chemistry, University of Padova, via Marzolo 1, 35131 Padova, Italy

S *Supporting Information*

ABSTRACT: Understanding the interaction of nanoparticles with cell membranes is a high-priority research area for possible biomedical applications. We describe our findings concerning the interaction of Au$_{144}$ monolayer-protected clusters (MPCs) with biomimetic membranes and their permeabilizing effect as a function of the transmembrane potential. We synthesized Au$_{144}$(SCH$_2$CH$_2$Ph)$_{60}$ and modified the capping monolayer with 8-mercaptooctanoic acid (Au$_{144}$OctA) or thiolated trichogin (Au$_{144}$TCG), a channel-forming peptide. The interactions of these MPCs with mercury-supported lipid mono- and bilayers were studied with a combination of electrochemical techniques specifically sensitive to changes in the properties of biomimetic membranes and/or charge-transfer phenomena. Permeabilization effects were evaluated through the influence of MPC uptake on the reduction of cadmium(II) ions. The nature and properties of the Au$_{144}$ capping molecules play a crucial role in controlling how MPCs interact with membranes. The native MPC causes a small effect, whereas both Au$_{144}$OctA and Au$_{144}$TCG interact significantly with the lipid monolayer and show electroactivity. Whereas Au$_{144}$OctA penetrates the membrane, Au$_{144}$TCG pierces the membrane with its peptide appendage while remaining outside of it. Both clusters promote Cd^{2+} reduction but with apparently different mechanisms. Because of the different way that they interact with the membrane, Au$_{144}$OctA is more effective in Cd^{2+} reduction when interacting with the lipid bilayer and Au$_{144}$TCG performs particularly well when piercing the lipid monolayer.
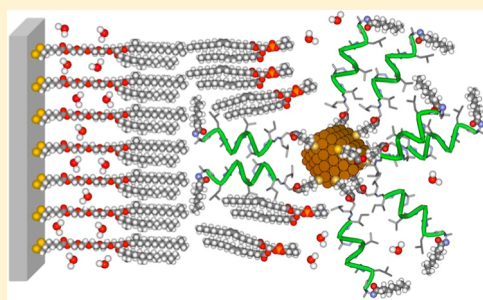
pplications of gold nanoparticles (AuNPs) are growing rapidly thanks to the unique optical and electronic properties of such materials.[1,2] AuNPs decorated by suitable molecules show properties that make them very interesting candidates in biomedicine.[3] In most applications, the nanoparticles are required to cross cell membranes either by endocytosis or direct penetration. The mechanisms by which AuNPs interact with cell membranes, however, are not completely understood, also because these processes depend on the nanoparticle size and the functional groups decorating the capping monolayer. The search for both critical particle sizes and morphology are thus of special significance and could be instrumental in devising suitable systems for nanomedicine applications.

The presence of a surface charge and its sign can dramatically influence the cellular uptake of AuNPs. Thus, 18 nm AuNPs were internalized into cancer cells more easily if positively charged with amino groups.[4] Similar conclusions were reached by modifying the monolayer of 13 nm AuNPs with PEG-NH$_2$ or PEG-COOH.[5] On the other hand, a study focusing on 1.6–5 nm AuNPs decorated by glucose, PEG-NH$_3^+$, glutathione, or mixtures of them provided evidence that gluthathione-coated AuNPs are the most efficiently internalized.[6] The internalization of 14–100 nm AuNP by HeLa cells is highly dependent upon their size and shape.[7] A study focusing on tiopronine-

protected AuNPs concluded that an endocytotic mechanism controls the transport of AuNPs in the endosome.[8] The internalization of tiopronine-protected 2–15 nm AuNPs showed that only those with a size of 2–6 nm were able to enter the cytoplasm and target the nucleus; the smaller AuNPs could enter by a diffusion mechanism.[9] The cellular uptake of gluthathione-protected 2 nm AuNPs was assessed by transmission electron microscopy imaging;[10] the core was described as Au$_{144}$, although the cluster having such a stoichiometry, also after ligand-place exchange reactions,[11,12] is described as having a diameter of 1.6 nm.[13] AuNPs (6 nm) coated with a mixture of hydrophobic and anionic thiolated ligands penetrate cell membranes with no evidence of membrane disruption and without requiring active endocytosis.[14]

Interactions between nanoparticles and cells can be influenced by various endogenous factors, which can be controlled by using biomimetic membranes. The penetration of 13 nm AuNPs into lysosomes was achieved by functionalizing the nanoparticles with both a cell-penetrating peptide and a lysosomal sorting peptide.[15] AuNP functionaliza-

tion with ligand/antibodies that specifically bind to membrane receptors/antigens[16] or the covalent binding of AuNPs to vesicles to be fused on cell membranes[17] are strategies adopted to immobilize nanoparticles on biomembranes. AuNPs (7−15 nm) captured in giant unilamellar vesicles, which are devoid of endocytotic capabilities, do not cross the vesicular membrane even after more than 72 h.[18] Single AuNPs were internalized into vesicles by guiding them with a laser light tuned to the plasmon resonance band of the AuNPs.[19] The disruption of a phosphatidylcholine monolayer by negatively charged protein-coated AuNPs was attributed to hydrophobic interactions.[20] AuNPs of ca. 2 nm and coated with an alkylamine substituent disrupt a mica-supported lipid bilayer primarily by expanding pre-existing defects.[21] Nanoparticles have also been incorporated into unilamellar vesicles: loading vesicles with 3 to 4 nm stearylamine-coated AuNPs increases their fluidity.[22] AuNPs (2 nm) coated with dodecanethiol were embedded into vesicles, and cryoTEM images showed that the resulting vesicles could be either fully loaded with nanoparticles or completely free of them.[23] A molecular dynamics simulation of the interactions of differently charged AuNPs with a negatively charged lipid bilayer pointed to a key role played by electrostatic interactions.[24]

On these grounds, it is quite evident that, despite important observations, the mechanism/s of AuNP interactions with cellular and biomimetic membranes is/are still poorly understood and sometimes controversial. Information concerning small AuNPs, i.e., those requiring a protecting molecular monolayer to prevent them from aggregation and growing into larger particles (monolayer-protected clusters, MPCs) is scarce. This is particularly true for the internalization of ultrasmall Au MPCs (<2 nm). In fact, to the best of our knowledge, penetration of ultrasmall gold MPCs into supported lipid bilayers and their permeabilizing effect as a function of the transmembrane potential have never been investigated. Our work is meant to be the first step in this direction. We used three MPCs composed of an Au_{144} core with a diameter of only 1.6 nm: this appears to be the smallest cluster with a definite size and stoichiometry, $Au_{144}(SR)_{60}$,[25] ever employed in studies focusing on the interaction of MPCs with membranes.

The three MPCs were $Au_{144}(SC_2H_4Ph)_{60}$ and two clusters obtained by ligand-place exchange with either a thiolated trichogin GA IV peptide (HS-TCG) to yield $Au_{144}(SC_2H_4Ph)_{48}(S\text{-}TCG)_{12}$ or 8-mercaptooctanoic acid (HS-OctA) to yield $Au_{144}(SC_2H_4Ph)_{29}(S\text{-}OctA)_{31}$. TCG is a lipopeptide antibiotic[26−28] consisting of a sequence of 10 amino acids and a lipophilic n-octanoyl group, and it displays a remarkable capability to modify the membrane permeability.[27,28] We added it to the MPC monolayer also because of our recent discovery that when TCG is incorporated into a mercury-supported tethered bilayer lipid membrane (tBLM) the latter is permeabilized at suitable potentials.[29] We studied the effect of these MPCs on two mercury-supported biomimetic membranes, namely, a lipid self-assembled monolayer (SAM) and a tBLM (Figure 1). The SAM consisted of a phospholipid monolayer (dioleoylphosphatidylcholine, DOPC). The tBLM was obtained by first tethering a thiolipid monolayer to the mercury surface. The thiolipid, called DPTL,[30] consists of a tetraethyleneoxy hydrophilic chain terminated at one end with a lipoic acid residue for anchoring to the mercury surface and covalently linked at the other end to two phytanyl chains mimicking the hydrocarbon tails of a lipid. The self-assembly of a DOPC monolayer on top of the thiolipid
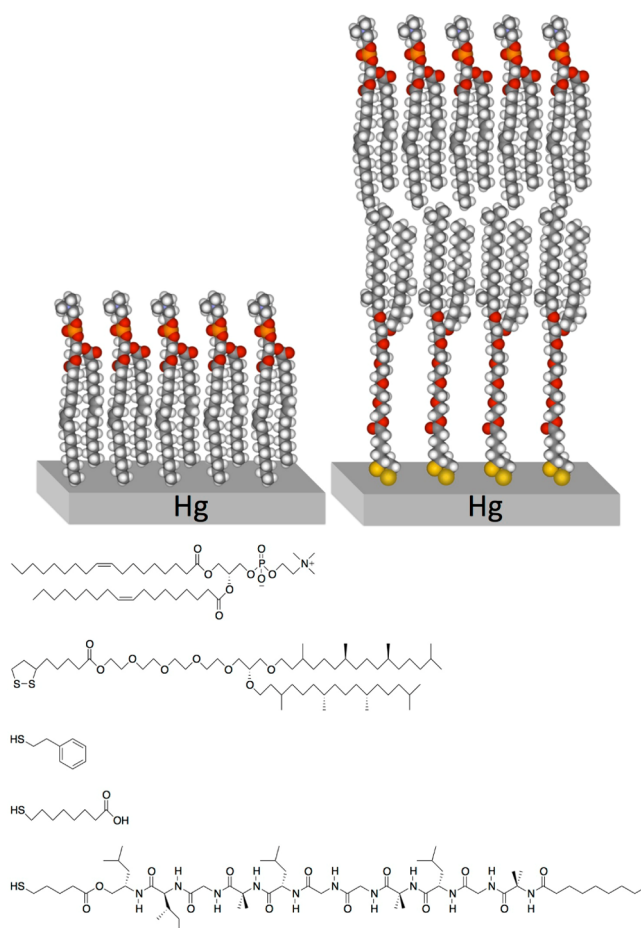

Figure 1. Schematic representation of the Hg-supported biomimetic membranes: DOPC monolayer (top left); tBLM composed of a DPTL monolayer covered with a DOPC monolayer (top right). Structures of (top to bottom) DOPC, DPTL, phenylethanethiol, HS-OctA, and HS-TCG.

monolayer gives rise to a lipid bilayer interposed between the aqueous solution and the hydrophilic chain region, which acts as an ionic reservoir.[29,31−34] In the present study, we devised a combination of electrochemical methods sensitive to changes in the properties of the biomimetic membranes and/or charge-transfer phenomena. We show that the nature and properties of the Au_{144} capping monolayer play important roles in controlling how the MPC interacts with membranes and the formation of charge-transfer pathways.

■ RESULTS

Synthesis and Characterization of the Au_{144} MPCs. The synthesis of $Au_{144}(SC_2H_4Ph)_{60}$ was carried out along the general lines described by Donkers et al.[13] The purified $Au_{144}(SC_2H_4Ph)_{60}$ clusters had the expected stoichiometry and optical and electrochemical properties.[12,13,25] The cluster monolayer was modified by ligand place exchange to introduce two thiolated molecules meant to provide affinity for membranes. To introduce a terminal carboxylic acid group, we used HS-OctA. The second thiol was based on TCG, an amphiphilic decapeptide containing three strongly helicogenic α-aminoisobutyric acid (Aib) residues (cf. Figure 1). Whereas the lipophilic n-octanoyl group at the N terminus is considered to be an important contribution for anchoring TCG to the hydrophobic part of the membrane bilayer, the C terminus

carries a 1,2-amino alcohol leucinol group. To keep TCG protruding from the MPC surface and thus being fully exposed to the solution, we reacted the peptide's leucinol OH with a thiolated tether, 5-mercaptopentanoic acid.

For both molecules, the exchange reaction was carried out for 24 h using a 1:1 molar ratio between the exogenous thiol (either HS-TCG or HS-OctA) and the phenylethanethiolate ligands. The average composition of the two exchanged clusters (hereafter denoted as $Au_{144}OctA$ and $Au_{144}TCG$) was assessed by ^1H NMR and thermogravimetric analysis (TGA). The first method is based on oxidatively decomposing the MPC with excess iodine and analyzing the molar ratio between the liberated ligands through a comparison between the integrals of conveniently separated peaks. The reaction was carried out in deuterated methanol. For $Au_{144}OctA$, we relied on the phenyl signal (for SC_2H_4Ph) and the resonance of the methylene adjacent to the carbonyl group (for S-OctA). Analysis (Figure S1) indicated that the extent of exchange was 52%. An independent determination of the monolayer composition was obtained by analysis of a high-resolution TGA trace. The desorption pattern was assigned, in comparison to the TGA pattern of the native $Au_{144}(SC_2H_4Ph)_{60}$ cluster, to the stepwise release of the two ligands (Figure S2). On the basis of this analysis, the estimated exchange was 51%, in full agreement with the ^1H NMR estimate. The same double analysis was carried out for $Au_{144}TCG$. By considering the integrals of distinct ^1H NMR signals in deuterated methanol belonging to either the thiolated TCG (methylene group adjacent to the tether's carbonyl) or phenylethanethiol (phenyl region) and assuming a 1:1 exchange, the extent of exchange was estimated to be 20% (Figure S3). As for the previous cluster, TGA shows separate desorption regions for the phenylethanethiolate- and the TCG-containing ligands (Figure S4). By assuming a 1:1 exchange, the estimated TCG exchange was 19%, once again in excellent agreement with the ^1H NMR analysis.

Whereas the composition of $Au_{144}OctA$ is straightforwardly established on a 1:1 exchange basis to be $Au_{144}(SC_2H_4Ph)_{29}(S-OctA)_{31}$, for $Au_{144}TCG$ a similar calculation requires some introductory comments. According to X-ray diffraction, NMR, FT-IR, and CD conformational studies, TCG is a helical peptide combining a distorted 3_{10}-helix with a longer segment of an irregular α-helix.[28] Because the IR absorption spectra of $Au_{144}TCG$ and trityl-protected S-TCG are very similar (Figure S5), it can be inferred that the helical structure of the peptide is not affected by binding to the gold core, as previously observed for thiolated Aib-oligopeptides capping MPCs of similar size.[35] Although the curvature of the gold core minimizes the steric hindrance between neighboring ligands,[36] the footprint of helical peptides is significantly larger than that of simpler molecular chains such as phenylethanethiol and S-OctA; however, the use of the sufficiently long thiolated tether, $-S-(CH_2)_4CO-$, in S-TCG is such to make the 1:1 exchange possible. To $Au_{144}TCG$ we can thus assign the average formula $Au_{144}(SC_2H_4Ph)_{48}(S-TCG)_{12}$. The different loading attained with the two ligands is attributed to the time allowed for the exchange to occur, shorter than that probably required to attain equilibrium exchange,[11] and also to the different size, shape, and self-aggregation properties of the two ligands used.[12]

Concerning the core of the exchanged MPCs, we checked the UV−vis pattern before and after exchange (Figure S6 and S7). The spectra of $Au_{144}OctA$ and $Au_{144}TCG$ maintain the same features of the native cluster; in particular, only a barely detectable shoulder is visible at 520 nm, i.e., where the surface

plasmon absorption of gold is expected to emerge as a band only for particles having diameters larger than ca. 2.4 nm.[37] This points to no size modification occurring during the exchange reaction, as previously observed for other exchange reactions on Au_{144}.[11,12] Transmission electron microcopy provides an average MPC size of 1.6 nm, in line with that of the native cluster (Figure S8). The MPCs were also characterized by differential pulse voltammetry (DPV). The DPV of $Au_{144}(SC_2H_4Ph)_{60}$ in CH_2Cl_2 is characterized by a sequence of charging steps with an average separation of 0.22 V, increasing to 0.28 V for low charging states.[12] The DPVs of $Au_{144}OctA$ and $Au_{144}TCG$ are very similar to that of the native cluster, as exemplified in Figure 2 for $Au_{144}(SC_2H_4Ph)_{29}(S-$
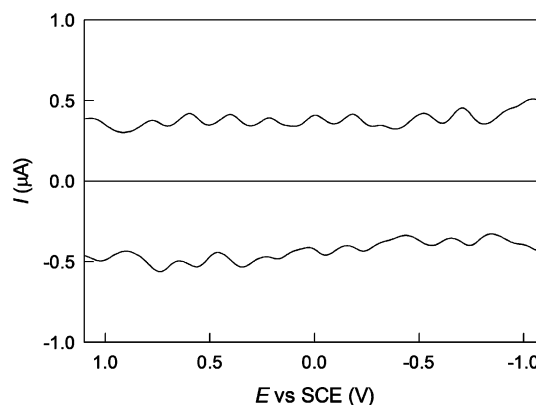

Figure 2. Differential pulse voltammetry of 0.26 mM $Au_{144}(SC_2H_4Ph)_{29}(S-OctA)_{31}$ obtained on a glassy carbon electrode in DMF/0.1 M TBAH at 25 °C. The top and the bottom traces correspond to the negative-going and positive-going DPV scans, respectively.

$OctA)_{31}$ in N,N-dimethylformamide (DMF) containing tetra-n-butylammonium hexafluorophosphate (TBAH). The average separation now is 0.19 V, in line with the expected effect exerted by a more polar solvent.[38,39] We note that the next known larger cluster is 2 nm $Au_{225}(SC_6H_{13})_{75}$,[40] which not only shows an average peak separation of 0.18 V in the less polar CH_2Cl_2 but also displays a broad shoulder at 520 nm, at variance with $Au_{144}(SC_2H_4Ph)_{60}$ and its exchanged derivatives. On these grounds, we can safely conclude that both exchanged clusters retained the original core size.

Effect of Au_{144} Clusters on a Mercury-Supported DOPC Monolayer. As detailed in the Supporting Information, a hanging mercury drop electrode (HMDE) is immersed in a 0.1 M KCl aqueous solution across a DOPC monolayer previously formed on top of the solution. The specific MPC solution is then injected into the latter. This procedure results in the formation of a DOPC monolayer or, after MPC injection, an MPC-modified DOPC monolayer on the HDME surface. The thus-modified electrodes are then used in a series of electrochemical experiments, such as AC voltammetry.

AC voltammetry consists of applying an AC voltage of small amplitude and given frequency to the electrochemical cell and recording the quadrature component of the current that flows through the cell with the same frequency. To record the current as a function of the applied potential E, the AC voltage is superimposed on a bias voltage that is varied linearly in time. The current is converted into the differential capacitance C by calibrating the instrument with a high-precision capacitor. If the adsorbed molecules do not undergo reorientation and no ion

movement across the lipid monolayer takes place, then the AC voltammogram is flat. Conversely, the reorientation of molecules changes their dipole moment normal component, and the potential difference thus generated must be compensated for by a flow of electrons along the external electric circuit to maintain the potential difference across the whole electrified interface constant. This causes a more or less intense pseudocapacitance peak in the AC voltammogram. The same considerations apply to ion movement across the monolayer.

In the absence of MPCs in solution, the C vs E curve for the DOPC-coated mercury electrode against E at 75 Hz exhibits a flat minimum of about 1.8 μF cm^{-2} between −0.3 and −0.8 V corresponding to a compact lipid monolayer impermeable to inorganic ions, followed by three pseudocapacitance peaks (black curve of Figure 3, which does not include the third, more
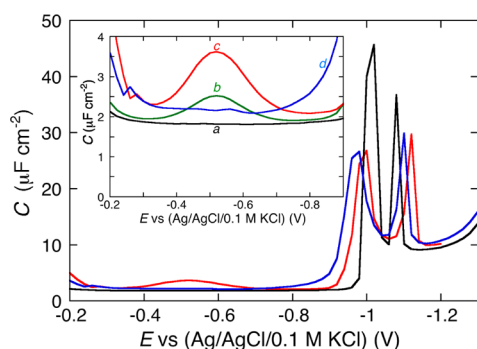

Figure 3. Curves of the differential capacitance C against the applied potential E at a mercury-supported DOPC monolayer in a pH 7 buffer solution of 0.1 M KCl in the absence of MPCs (black curve) and in the presence of 2 μg mL^{-1} Au$_{144}$OctA (red curve) or 2 μg mL^{-1} Au$_{144}$TCG (blue curve). The C vs E curve in the presence of 2 μg mL^{-1} Au$_{144}$(SC$_2$H$_4$Ph)$_{60}$ is not shown because it does not affect the two pseudocapacitance peaks. The inset shows an expanded view of the flat region of the C vs E curves for DOPC alone (a) and in the presence of 2 μg mL^{-1} Au$_{144}$(SC$_2$H$_4$Ph)$_{60}$ (b), Au$_{144}$OctA (c), or Au$_{144}$TCG (d).

cathodic peak). Proceeding toward more negative potentials, the first two peaks are due to a cooperative reorientation of the lipid molecules, while the third peak is due to their partial desorption.[41] The first peak results from surface defects that allow virtually uninhibited access of inorganic ions to the mercury surface, whereas the second peak results from the nucleation and growth of the defects formed at the first peak, causing their coalescence.

As a rule, molecules capable of penetrating the hydrocarbon tail region of the phospholipid monolayer increase its capacitance over the potential range of the flat capacitance minimum with respect to the value of 1.8 μF cm^{-2} observed in the absence of foreign species, if their polarizability is appreciably higher than that of the lipid molecules. Conversely, they affect the monolayer capacitance only slightly if they have a low polarizability.[42] In both cases, if the concentration of exogenous molecules in the lipid monolayer is sufficiently high, then their intercalation with the lipid molecules prevents the latter from undergoing a sufficiently sharp cooperative reorientation, thus broadening and depressing the two pseudocapacitance peaks in the black curve of Figure 3. On the other hand, molecules adsorbed on top of the lipid monolayer but unable to penetrate it alter and depress the

pseudocapacitance peaks by interacting with the polar heads.[43] Such molecules may also decrease the capacitance over the potential range of the flat capacitance minimum if they form a sufficiently compact layer, thereby increasing the thickness of the whole adsorbed material.

Capacitance vs potential curves of the Hg-supported DOPC monolayer were recorded in the presence of 2 μg mL^{-1} of each of the three MPCs (Figure 3). Whereas Au$_{144}$OctA and Au$_{144}$TCG broaden and depress the two pseudocapacitance peaks in the potential region from −0.9 to −1.15 V, Au$_{144}$(SC$_2$H$_4$Ph)$_{60}$ has no effect on them. The inset illustrates further details. The curves in the presence of Au$_{144}$(SC$_2$H$_4$Ph)$_{60}$ and Au$_{144}$OctA show a rounded maximum at around −0.50 V. The capacitance in the presence of Au$_{144}$(SC$_2$H$_4$Ph)$_{60}$ coincides with that of the sole DOPC on the two sides of the maximum, whereas that in the presence of Au$_{144}$OctA remains slightly higher. The curve in the presence of Au$_{144}$TCG shows no maximum, is higher than that of the sole DOPC, and increases appreciably at potentials negative of −0.8 V.

The fact that Au$_{144}$(SC$_2$H$_4$Ph)$_{60}$ does not affect the two pseudocapacitance peaks in Figure 3 indicates that it does not interact with the polar heads of DOPC. Its effect on the flat region of the C vs E curve is also very small and is confined to a potential range straddling −0.50 V, where a small hump develops. Evidently, the interaction of Au$_{144}$(SC$_2$H$_4$Ph)$_{60}$ with the flat region of the AC voltammogram is so weak and determined by such a low number of MPCs in the SAM that it is not sufficient to hamper the cooperative reorientation of the DOPC molecules responsible for the pseudocapacitance peaks. Conversely, Au$_{144}$OctA and Au$_{144}$TCG interact more strongly with the SAM, as they affect the flat region of the C vs E curve more pronouncedly and depress and alter the DOPC pseudocapacitance peaks.

To gain insights into the nature of the interaction of the three MPCs with the DOPC SAM, electrochemical impedance spectroscopy (EIS) was employed. This technique consists of applying at each potential E a small AC voltage of frequency f varying progressively over a maximum range of 10^{-3} to 10^5 Hz and measuring both the amplitude and the phase shift of the resulting current flowing at the same frequency. These two quantities yield the complex admittance Y, which can be roughly compared to the conductance G in direct current measurements. The reciprocal of the complex admittance Y is the complex impedance Z. For a parallel combination of a resistance R and a capacitance C (RC mesh), the corresponding complex admittance is given by $Y = Y' - iY'' = G - i2\pi f C$, where i is the imaginary unit. In our experiments, the EIS measurements covered a frequency range from 0.1 to 10^5 Hz and a potential range from −0.3 to −0.8 V. The plot of Y' against E at 10 Hz for a DOPC monolayer in the presence of Au$_{144}$OctA or Au$_{144}$TCG attains a maximum in the vicinity of −0.45 V and tends to merge with that of the sole DOPC on both sides of the maximum (see curves a and b in Figure 4, in which Y' is plotted after subtracting the highly reproducible Y' vs E data of the sole DOPC). These maxima indicate that both MPCs significantly interact, to different extents, with the DOPC monolayer. Conversely, the Y' vs E plot in the presence of Au$_{144}$(SC$_2$H$_4$Ph)$_{60}$ is virtually coincident with that in its absence. This indicates that whereas Au$_{144}$OctA and Au$_{144}$TCG conduct the current across the DOPC monolayer, Au$_{144}$(SC$_2$H$_4$Ph)$_{60}$ does not. This conductance is quite probably due to a flow of electrons between the MPCs incorporated into the lipid film and the metal; appreciable ion
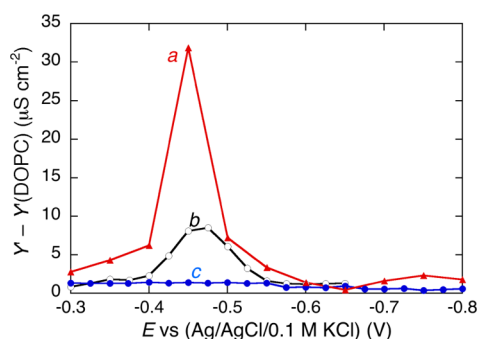
Figure 4. Curves of the in-phase component Y' of the admittance against E at a mercury-supported DOPC monolayer in a pH 7 buffer solution of 0.1 M KCl in the presence of 2 μg mL^{-1} Au$_{144}$OctA (a), Au$_{144}$TCG (b), and Au$_{144}$(SC$_2$H$_4$Ph)$_{60}$ (c). The curves were obtained after the subtraction of the curve of the sole DOPC.

movement across the lipid film can be discarded because of the lack of an ionic reservoir between the DOPC monolayer and the mercury surface.

The behavior of the DOPC SAM was also investigated by cyclic voltammetry (CV). We will first describe the effect of Au$_{144}$OctA, followed by that of Au$_{144}$TCG. Figure 5 shows the
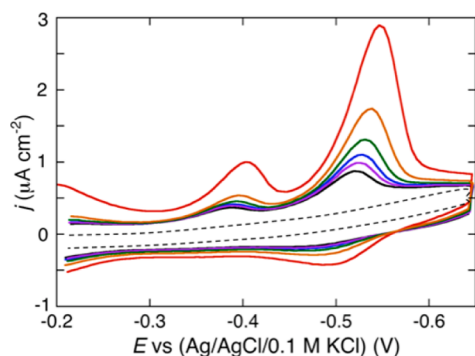

Figure 5. Cyclic voltammograms at a mercury-supported DOPC monolayer in a pH 7 buffer solution of 0.1 M KCl and 4 μg mL^{-1} Au$_{144}$OctA recorded at progressively increasing times. The peak currents decrease as the time increases. Scan rate = 50 mV s^{-1}. The dashed curve is the cyclic voltammogram of the DOPC SAM in the absence of Au$_{144}$OctA.

CV curves recorded during a series of voltage cycles at an Hg-supported DOPC monolayer in a solution containing 4 μg mL^{-1} Au$_{144}$OctA. The CV curves, which span the potential range of stability of the SAM (-0.2 V > E > -0.65 V), are not consecutive. Rather, from a whole set of consecutive cycles, a series of CV curves corresponding to progressively increasing times were selected in such a way as to illustrate their progressive evolution. The CV pattern shows two broad cathodic peaks at about -0.40 and -0.55 V and a smaller anodic rounded hump at about -0.50 V. Repeated voltage cycles cause a rapid decrease in the current density (j) of the two cathodic peaks and the anodic hump, which in a short time becomes vanishingly small.

As distinct from EIS, CV is not phase-sensitive and thus it is impossible to establish whether the hump and the peaks in Figure 5 are due to the reorientation of adsorbed molecules, ion movement, or electron transfer (ET). However, a judicious choice of the different electrochemical techniques may help to clarify this point. To this end, we used potential step

chronocoulometry, which consists of stepping E between two selected values and recording the charge flowing as a consequence of this potential jump as a function of time. Figure 6 shows a series of charge transients recorded at the
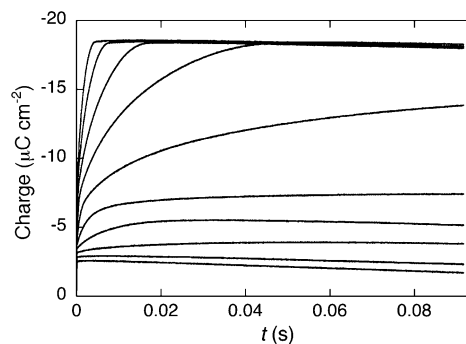

Figure 6. Curves of the charge density Q against time t following potential jumps from -0.20 V to progressively more negative final potentials E_f at a mercury-supported DOPC monolayer in a pH 7 buffer solution of 0.1 M KCl and 4 μg mL^{-1} Au$_{144}$OctA. The absolute value of Q increases progressively as E_f varies from -0.35 to -0.80 V by -50 mV potential increments.

same DOPC monolayer as in Figure 5 by stepping the potential from a fixed value of -0.2 V to progressively more negative final values E_f. The charge density (Q) becomes practically independent of time for $t > 0.02$ s over the potential range straddling the two cathodic voltammetric peaks of Figure 5. A further increase in E_f causes the charge to increase rapidly in time until it attains an almost constant limiting value of about -18.5 μC cm^{-2} for $E_f \leq -0.65$ V. More precisely, with a negative shift in E_f, this limiting value continues to increase gradually but only by a very small amount such as to be practically imperceptible in the last four charge transients in Figure 6. This further slight increase in charge is due to a pure capacitive contribution, whereas the reproducible charge of -18.5 μC cm^{-2} may be ascribed either to a movement of charge or to an ET from Hg to a well-defined amount of Au$_{144}$OctA incorporated into the DOPC SAM. Clear evidence that this charge is due to the complete desorption of negatively charged Au$_{144}$OctA MPCs was provided by carrying out the same CV measurements of Figure 5 in an unbuffered solution of 0.1 M KCl, whose measured pH was ~5.

The CV pattern of a DOPC monolayer in a pH 5 unbuffered solution of 0.1 M KCl and 4 μg mL^{-1} Au$_{144}$OctA is practically featureless. This difference in behavior is ascribable to the clustered carboxyl groups being almost completely protonated at this pH, whereas they are partially deprotonated at pH 7. In this connection, it should be noted that the intrinsic pK_a of clustered carboxyl groups is much higher than that of free carboxylic acids due to the mutual electrostatic repulsion between neighboring carboxylate groups. Smalley et al. reported a pK_a value of 5.7 $\pm$ 0.2 for 11-mercaptoundecanoic acid on gold at 0.10 M ionic strength.[44] The pK_a values of SAMs of different COOH-terminated alkanethiols on gold were reported to be larger by about 3 pK_a units than those for free thiols,[45] although the passage from the totally protonated to the totally deprotonated forms was sometimes found to be not as sharp as expected. After Au$_{144}$OctA incorporation, increasing the solution pH from 5 to 7 has no effect on the CV behavior. This indicates that the neutral Au$_{144}$OctA MPCs incorporated

into the DOPC monolayer at pH 5 have no tendency to be desorbed and to undergo deprotonation at pH 7.

To confirm that $Au_{144}OctA$ undergoes incorporation into the DOPC SAM not only at pH 7 but also at pH 5, the effect of this MPC on the permeabilization of the lipid monolayer toward cadmium ions was investigated at both pH values. The cadmium ion is reduced reversibly on bare mercury with a formal potential of −0.646 V in 0.1 M KCl, but its electroreduction with amalgam formation is completely blocked on DOPC-coated mercury at potentials positive of −0.8 V.[34] The alternative choice of Tl^+, which is reduced reversibly on bare mercury in the middle of the potential range of stability of the DOPC monolayer with a formal potential of −0.47 V, was discarded because of a lower blocking effect of the DOPC monolayer toward this monovalent cation. The addition of 4 μg mL^{-1} $Au_{144}OctA$ to a Hg-supported DOPC monolayer in a pH 7 aqueous solution of 0.1 M KCl and 6×10^{-5} M $CdSO_4$ yields, after repeated voltage cycles, a highly irreversible CV pattern (curve f in Figure 7). The CV curve shows an oxidation peak at
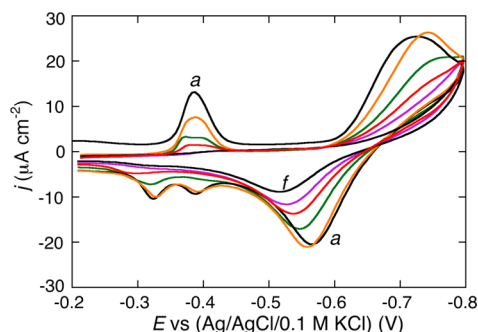

Figure 7. Cyclic voltammograms at a mercury-supported DOPC monolayer in a pH 7 buffer solution of 0.1 M KCl containing 4 μg mL^{-1} $Au_{144}OctA$ and 6×10^{-5} M $CdSO_4$, as recorded at progressively increasing times after keeping the electrode under open circuit conditions for a few minutes (see the text). The cyclic voltammograms evolve from curve a to curve f as time increases. Scan rate = 50 mV s^{-1}.

about −0.5 V and a reduction current that does not reach the corresponding peak current at the most negative potential explored, i.e., −0.8 V. A practically identical CV pattern was obtained in a pH 5 unbuffered solution, demonstrating that $Au_{144}OctA$ is incorporated into the DOPC monolayer even at pH 5.

Having clarified the nature of the anodic hump and the two cathodic peaks at pH 7 in Figure 5, it remains to be explained why each anodic hump is smaller than the two cathodic peaks recorded during the immediately preceding negative voltage scan. One reason is that, during a positive scan, the number of MPCs readsorbed is always smaller than the number desorbed during the preceding negative scan, as appears from the progressive decrease in the peaks with an increase in the number of voltage cycles. In addition, the transient hole that the desorbing nanoclusters are leaving in the DOPC monolayer during their desorption is likely to cause a small concomitant flow of K^+ ions toward the negatively charged electrode surface. This would cause a further electron flow to the electrode surface along the external circuit and a resulting increase in the cathodic peaks. A similar small flow of K^+ toward the electrode during the beginning of $Au_{144}OctA$ readsorption may contribute to the decrease in the anodic current hump, further enhancing the difference in size between this hump and the

immediately preceding cathodic peaks. It should be noted that any defect temporarily induced by the incorporation of the MPCs in a mercury-supported DOPC SAM is spontaneously and rapidly healed by the lipid molecules over the whole potential range of stability of the monolayer, thanks to their fluidity and lateral mobility on this liquid metal.

Further confirmation of the complete desorption of the $Au_{144}OctA$ MPCs at potentials negative of −0.7 V comes from the AC voltammogram of the DOPC SAM in the presence of 2 μg mL^{-1} $Au_{144}OctA$ (curve c in the inset of Figure 3), which tends to merge with that in the absence of the nanoclusters, pointing to $Au_{144}OctA$ release from the hydrocarbon tail region. The further increase in C toward more negative potentials, with a depression of the two pseudocapacitance peaks, denotes the interaction of the desorbed $Au_{144}OctA$ MPCs with the polar head region.

The CV curve f in Figure 7, as obtained after repeated voltage cycles at a DOPC SAM at both pH 5 and 7, exhibits a peculiar behavior at pH 7 but not at pH 5. Thus, if this DOPC SAM at pH 7 is left for a few minutes under open-circuit conditions and a new series of voltage cycles is started, the CV curve of the cadmium ion is initially higher and quasireversible, with a cathodic peak potential of −0.73 V (Figure 7, curve a). Moreover, the CV curve also shows an additional cathodic hump at about −0.39 V and two corresponding anodic humps at about −0.39 and −0.32 V. Repeated voltage cycling determines a rapid evolution in the features of the Cd^{2+} CV, as shown in Figure 7 when passing from the solid curve a to the solid curve f. Thus, the cathodic hump and the two corresponding anodic humps decrease gradually, while the CV curve ascribable to direct Cd^{2+} electroreduction becomes progressively more irreversible. Ultimately, the three humps vanish and the CV curve coincides with that obtained before the rest time of the DOPC monolayer under open-circuit conditions. It is worth noting that the above behavior is entirely reproducible. The fact that this behavior is not observed at pH 5 strongly suggests that it is somehow related to the negative charge of the MPCs at pH 7. In a different series of measurements, repeated voltage cycling immediately after a rest time under open-circuit conditions was performed between −0.20 and −0.65 V (Figure 8) so as to avoid Cd^{2+} electroreduction at $E < −0.65$ V. In this case, a cathodic peak at about −0.40 V and a corresponding anodic peak, both flanked by a small shoulder, are obtained. Instead of decreasing, the two peaks increase during repeated voltage cycling.
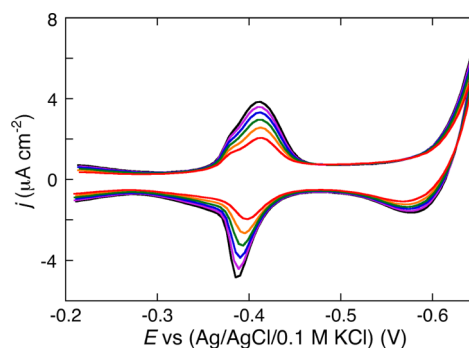

Figure 8. Cyclic voltammograms recorded at progressively increasing times under the same experimental conditions as in Figure 7, except for scanning the potential between −0.20 and −0.65 V. Progressive voltage cycling causes the current to increase. Scan rate = 50 mV s^{-1}.

Let us now consider the effect of adding $Au_{144}TCG$. The CV curve of a DOPC monolayer in a pH 7 buffer solution of 0.1 M KCl containing $Au_{144}TCG$ shows a cathodic peak at about −0.47 V and a corresponding anodic peak (Figure S9). The addition of 6×10^{-5} M $CdSO_4$ to a pH 7 buffer solution of 0.1 M KCl and 4 μg mL^{-1} $Au_{144}TCG$ in contact with the DOPC monolayer yields a remarkable quasireversible CV curve after a few voltage cycles, as shown by curve b of Figure 9. The height
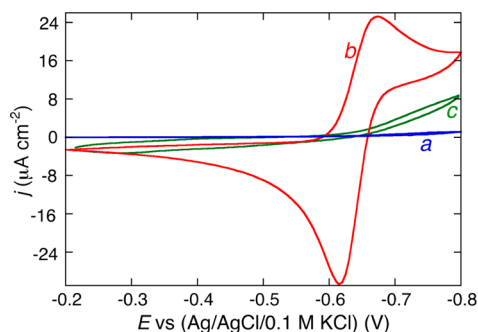

Figure 9. Cyclic voltammograms at a mercury-supported DOPC monolayer in a pH 7 buffer solution of 0.1 M KCl and 6×10^{-5} M $CdSO_4$ in the absence of MPCs (a) and in the presence of 4 μg mL^{-1} $Au_{144}TCG$ (b) or $Au_{144}(SC_2H_4Ph)_{60}$ (c). Scan rate = 50 mV s^{-1}.

of the voltammetric peaks is about 70% of that observable on bare mercury, and the separation between the oxidation and reduction peaks amounts to 50 mV, not far from the value of 30 mV expected for a Nernstian two-electron transfer.[46] Unlike $Au_{144}OctA$, the $Au_{144}TCG$ and $Au_{144}(SC_2H_4Ph)_{60}$ MPCs have no ionizable groups and therefore are not expected to be affected by pH changes.

As opposed to $Au_{144}OctA$ and $Au_{144}TCG$, the incorporation of the native, fully hydrophobic cluster $Au_{144}(SC_2H_4Ph)_{60}$ in the DOPC monolayer from its 4 μg mL^{-1} solution in aqueous 0.1 M KCl has practically no effect on the featureless cyclic voltammogram of the monolayer recorded between −0.2 and −0.8 V. Moreover, it has an almost negligible permeabilizing effect on Cd^{2+}, as shown by the CV curve of 6×10^{-5} M $CdSO_4$ in Figure 9, curve c.

Effect of Au_{144} Clusters on a Mercury-Supported DPTL|DOPC Bilayer. The procedure used to prepare the tBLM, whose details are described in the Supporting Information, consists of tethering a SAM of DPTL to a mercury electrode. A DOPC monolayer is then self-assembled on top of the DPTL monolayer by immersing the DPTL-coated mercury electrode into a pH 7 working solution of 0.1 M KCl, on whose surface a DOPC film has been previously spread. MPCs and/or $CdSO_4$ are/is injected into the working solution only after the formation of the DPTL|DOPC bilayer (the tBLM).

By stirring a pH 7 buffer solution of 0.1 M KCl and 4 μg mL^{-1} $Au_{144}OctA$ in contact with a DPTL|DOPC tBLM and carrying out multiscan CV between −0.2 and −1.2 V, no detectable effect of this MPC was observed, as indicated by the virtual superimposition of the curves recorded in the absence and in the presence of the MPC. On the other hand, by repeating this procedure after the addition of 6×10^{-5} M $CdSO_4$, the CV curve a in Figure 10 was obtained after reaching a steady state. This CV curve shows a cathodic peak at −0.99 V and an anodic peak at −0.31 V. The midpoint between these two peaks, −0.65 V, is very close to the formal potential,
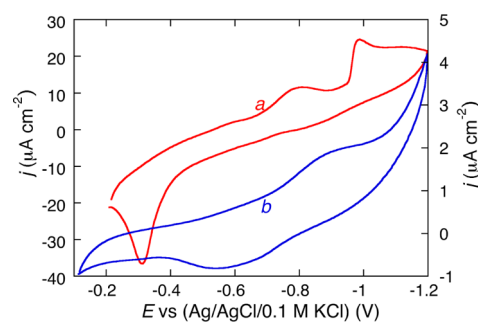

Figure 10. Cyclic voltammograms at a mercury-supported DPTL| DOPC tBLM in a pH 7 buffer solution of 0.1 M KCl and 6×10^{-5} M $CdSO_4$ containing 6 μg mL^{-1} $Au_{144}OctA$ (a) or $Au_{144}TCG$ (b). The left-hand current scale refers to curve a, and the right-hand scale refers to curve b. Scan rate = 50 mV s^{-1}.

−0.646 V, of the $Cd^{2+}/Cd(Hg)$ couple on bare mercury, pointing to a highly irreversible CV curve of the cadmium ion. The additional current hump at about −0.8 V can be tentatively ascribed to a catalytic effect of $Au_{144}OctA$ (Discussion). If after attaining this irreversible CV by continuous potential cycling between −0.2 and −1.2 V the potential is repeatedly scanned in the smaller potential range from −0.2 to −0.8 V, the CV curve decreases rapidly in height and eventually vanishes. It is worth mentioning that the potential range from −0.2 to −0.8 V corresponds to the range of physiological transmembrane potentials, while the range from −0.2 to −1.2 V is significantly larger. In fact, the electric potential E can be related to the corresponding transmembrane potential ϕ_{lb}, namely, the potential difference across the lipid bilayer moiety of the tBLM. In the absence of ion channels in the lipid bilayer moiety and hence in the absence of ions in the tetraethyleneoxy hydrophilic spacer, ϕ_{lb} can be estimated from equation $\phi_{lb} = 0.72 \times (E \text{ vs Ag}|\text{AgCl}|0.1 \text{ M KCl}) + 0.520 \text{ V})$, which we derived on the basis of an approximate extra-thermodynamic procedure.[47] To take place, the permeabilizing effect of $Au_{144}OctA$ toward Cd^{2+} electroreduction thus requires the application of nonphysiological transmembrane potentials.

Analogous conclusions can be drawn for 4 μg mL^{-1} $Au_{144}TCG$, which also has no detectable effect on the CV of a DPTL|DOPC tBLM in a pH 7 buffer solution of 0.1 M KCl. The addition of 6×10^{-5} M $CdSO_4$ followed by multiscan CV between −0.1 and −1.2 V yields CV curve b in Figure 10, which, however, is characterized by a much smaller current than observed in the presence of $Au_{144}OctA$. As for the latter MPC, subsequent repeated voltage scans between −0.2 and −0.8 V make the effect of $Au_{144}TCG$ vanish.

The electrochemical impedance pattern of the DPTL|DOPC tBLM is not affected by the incorporation of $Au_{144}OctA$ and $Au_{144}TCG$ nanoparticles. Conversely, however, $Au_{144}(SC_2H_4Ph)_{60}$ increases the conductance and the capacitance of the tBLM to some extent (Figures S10 and S11). These effects suggest a deeper penetration of the highly hydrophobic phenylated nanocluster into the lipid monolayer moiety of DPTL, with respect to the other two MPCs.

■ DISCUSSION

In organic solvents, Au_{144} MPCs behave as multivalent redox species, qualifying them as quantum capacitors (cf. Figure 2).[1a,12] In aqueous solution, the electrochemical behavior of films of this class of MPCs shows that the presence and position of redox peaks depend on the electrolyte.[48−50] No

G
dx.doi.org/10.1021/la500909j | Langmuir XXXX, XXX, XXX−XXX

cathodic peaks are observed, an intriguing feature that is difficult to understand.[51] Moreover, because of the high dielectric constant of the medium, the peaks are also less resolved than in organic solution.[1a] This phenomenon is evident even for the smaller $Au_{25}(SR)_{18}$ cluster, which displays molecule-like properties including very nice and well-separated voltammetric peaks in organic solvents[38,52,53] but only a poorly resolved, broad peak in aqueous solution.[54] In our hands, we consistently detect a peak associable with MPC charging at ca. −0.45 V. Interestingly enough,[48−50] what we observe is a cathodic peak. Even though the dipole moments of the molecules capping the MPC may affect the electrochemical behavior,[12] in the present case this effect seems small. This is confirmed by the presence of a peak at around −0.45 V, for both $Au_{144}OctA$ and $Au_{144}TCG$, in the Y' vs E curves (Figure 4), which are a rough measure of the conductance of the DOPC monolayer. We thus ascribe this peak to a continuous hopping of one electron from each MPC incorporated into the lipid monolayer to the electrode and vice versa, following the AC signal. The peak lies close to the potential at which the film pressure of the DOPC SAM on Hg attains a maximum value and hence where the stability of this monolayer relative to its displacement by water is also a maximum.[41] This excludes the possibility of the exchange of electrons between the MPCs and the metal being related to a decreased stability of the DOPC monolayer. From the maximum conductance, 32 $\mu S\ cm^{-2}$, of the DOPC SAM incorporating $Au_{144}OctA$ (Figure 4), we estimate the number density N of this MPC at 6.4×10^{10} molecules cm^{-2}.[55] Agreement with the experimental conductance in Figure 4 is attained by ascribing a value of ca. 1% to the surface coverage by $Au_{144}OctA$. A current peak at about −0.40 V is also observed in the CV curves of the DOPC monolayer in the presence of $Au_{144}OctA$, as shown in Figure 5. The charge under this peak in the first CV trace of Figure 5 amounts to about 0.5 $\mu C\ cm^{-2}$ and is therefore definitely too high to be ascribed to one electron per each incorporated $Au_{144}OctA$ MPC. In fact, if this were the case, then the number density N of the MPCs in the DOPC monolayer would be equal to $Q/e = (0.5/1.6 \times 10^{-13}) = 3.1 \times 10^{12}$ molecules cm^{-2}, which corresponds to a surface coverage of about 56%. This charge is probably related to the negative charge of $Au_{144}OctA$ at pH 7, which is likely to be much less than its maximum value of 31 electron charges per MPC. An increase in this negative charge by one unit, following the uptake of one electron per MPC, may induce a partial desorption of the nanoclusters from inside the hydrocarbon tail region. This would be accompanied by a concomitant flow of electrons along the external circuit to the mercury surface to maintain the electroneutrality of the whole electrified interface. Complete desorption of the MPCs takes place in connection with the more cathodic CV peak at ca. −0.54 V in Figure 5. This is confirmed by the chronocoulometric charge transients in Figure 6, whose maximum limiting charge increases almost imperceptibly by the sole purely capacitive contribution at potentials negative of −0.65 V.

The effect of the $Au_{144}OctA$ MPCs on Cd^{2+} reduction is puzzling. During the first series of voltage cycles following the addition of the MPCs and cadmium ions to the solution in contact with a freshly formed DOPC monolayer, Cd^{2+} gradually penetrates the monolayer, partially disrupted by the adsorbed MPCs, in a nonspecific manner. Eventually, the highly irreversible CV in Figure 7 (curve f) is obtained. During the subsequent rest time under open circuit conditions, we may hypothesize a closer approach of the nanoclusters to the mercury surface, no longer hampered by electrostatic repulsion from a negatively charged electrode and possibly favored by further monolayer disruption produced by Cd^{2+} penetration. At the beginning of the second series of voltage cycles, the $Au_{144}OctA$ MPCs are in a position to exert a catalytic effect on Cd^{2+} reduction. By catalytic effect, we mean an enhancing effect requiring direct contact between the catalyst (in the present case, the MPC) and the substrate. This effect is observed around the peak associated with MPC charging and involves the uptake of an electron from the mercury by each MPC, which then releases it to one Cd(II) or Cd(I) ion. This process, which generates a cathodic peak at about −0.39 V, requires close contact between the MPCs and cadmium ions, which are expected to move along the side of the nanoclusters, where the monolayer structure is probably more disrupted, until they reach the mercury surface in the Cd(0) state. An MPC-mediated ET across the lipid monolayer can be excluded because we verified that $Au_{144}OctA$ does not promote $Ru(NH_3)_6^{3+}$ electroreduction to $Ru(NH_3)_6^{2+}$, which takes place reversibly on bare mercury with a formal potential of −0.220 V.

The positive voltage scan gives rise to two anodic peaks at −0.39 and −0.32 V (cf. Figure 7, curve a), which can be tentatively ascribed to Cd(I) and Cd(II) formation, again catalyzed by the $Au_{144}OctA$ MPCs. These nanoclusters also exert an indirect enhancing effect on the conventional Cd^{2+} CV curve, which is higher than curve f obtained before the rest time under open circuit conditions and exhibits an electroreduction peak at about −0.73 V. However, progressive $Au_{144}OctA$ desorption following repeated voltage cycles wipes out the catalytic effect, ultimately again yielding the highly irreversible CV curve f. If this desorption is avoided by selecting a narrower potential range, then the catalytic effect on Cd^{2+} reduction and $Cd^0(Hg)$ oxidation around the formal potential associated with the MPC increases with increasing voltage cycling, as shown in Figure 8.

The behavior of $Au_{144}TCG$ toward the Hg-supported DOPC monolayer is quite different from that of $Au_{144}OctA$. The small effect of $Au_{144}TCG$ along the potential range of the flat capacitance minimum of the lipid monolayer (blue curve in Figure 3) excludes an appreciable MPC penetration into the hydrocarbon tail region, i.e., near the electrode surface. On the other hand, its depressive effect on the pseudocapacitance peaks beyond −0.9 V denotes a strong interaction of $Au_{144}TCG$ with the polar head region of DOPC. This behavior can be explained by considering that the TCG lipopeptaibol may easily penetrate both lipid monolayers[56] and bilayers.[29] Likewise, the TCG residues capping $Au_{144}TCG$ may pierce the lipid monolayer and thus anchor the MPC to it, which would prevent MPCs' incorporation into the hydrocarbon tail region. Nonetheless, the conductance peak in Figure 4 (curve b) and the cathodic and anodic peaks in the CV curve of Figure S9, all occurring around −0.47 V, strongly suggest that, despite not penetrating the DOPC monolayer, the $Au_{144}TCG$ nanoclusters may still exchange electrons with mercury at virtually the same MPC formal potential observed for $Au_{144}OctA$. This important feature can be tentatively explained by assuming that electrons may flow along the TCG helixes spanning the lipid monolayer. This is indeed conceivable due to the 3_{10}-helical component of the TCG secondary structure and the fact that 3_{10}-helices display outstanding properties as ET mediators.[57,58] In turn, this would also imply an actual piercing of the SAM by the

TCG helix, not just the occurrence of a carpet-like interaction in which the peptide helices float on the SAM with only their hydrophobic part actually penetrating it.[59] No desorption peak is shown by the CV curve in Figure S9, which is in keeping with the fact that Au_{144}TCG is uncharged and hence not electrostatically repelled by the negatively charged metal surface. The modest disruption produced by the TCG helixes and by few, if any, nanoclusters penetrating the hydrocarbon tail region may cause at most a small nonspecific flux of K^+ toward the electrode; this allows the anodic peak in Figure S9, due to electron flow from the MPCs to the electrode, to be more clearly visible and more stable than the anodic hump in the CV curves for Au_{144}OctA of Figure 5.

Besides the different way in which the two MPCs interact with the monolayer, Au_{144}TCG is also more effective than Au_{144}OctA at promoting Cd^{2+} electroreduction, inasmuch as it yields the nice quasireversible CV shown by curve b in Figure 9. This is a truly remarkable feature. The TCG helixes that penetrate the DOPC monolayer and cause a small increase in capacitance throughout the whole potential range of the flat capacitance minimum (curve d in the inset of Figure 3) must play some role in the permeabilization of the lipid monolayer toward Cd^{2+}. Molecular-view interpretations include the formation of a channel-forming bundle of TCG residues provided by a single MPC, which would imply phase separation on the MPC surface, as already discussed, or clustering of neighboring nanoclusters.

Concerning the hydrophobic $Au_{144}(SC_2H_4Ph)_{60}$, its incorporation into the DOPC monolayer is revealed primarily by the capacitance maximum centered at about −0.50 V in the inset of Figure 3, curve b. The fact that its presence does not affect the two pseudocapacitance peaks, however, indicates that the number of these MPCs in the lipid monolayer is not sufficient to hamper the cooperative reorientation of the DOPC molecules responsible for the pseudocapacitance peaks. Besides, this MPC is virtually apolar and has very low polarizability, which are features expected to impart a stealth effect on the membrane. A small number of these MPCs is also confirmed by the very small permeabilization of the lipid monolayer toward Cd^{2+}, as appears from curve c in Figure 9. Finally, we should also note that $Au_{144}(SC_2H_4Ph)_{60}$ is larger (~3.2 nm)[12] than the DOPC monolayer thickness (~2.3 nm)[60] and thus cannot be easily stabilized by both the membrane and the surrounding medium: this is at variance with the modified clusters, which possess functional groups allowing them to interact with both phases, albeit with different mechanisms.

CONCLUSIONS

Electrochemical analysis indicates that the three MPCs investigated interact with biomimetic membranes by different mechanisms. The native, strongly hydrophobic $Au_{144}(SC_2H_4Ph)_{60}$ cluster causes a very small effect on the DOPC SAM but, not unexpectedly, penetrates the tBLM more deeply. Conversely, both Au_{144}OctA and Au_{144}TCG interact with the DOPC monolayer and show electroactivity. Au_{144}TCG pierces the membrane with its peptide appendage while remaining outside of it. In this position, it may transfer electrons between its gold core and the electrode across the membrane, with a possible active role played by the helices piercing the monolayer. Au_{144}OctA penetrates the monolayer, at least as far as its diameter of ~4 nm permits. In its negatively charged form, this MPC mediates ET between an electroactive cation such as Cd^{2+} and the electrode via its effective redox

potential, thereby allowing its translocation across the membrane. This is possible through both the DOPC monolayer and the tBLM. That Au_{144}TCG is less efficient toward the latter can be explained by considering that Au_{144}TCG gets trapped on the membrane surface and thus the TCG chain can span only half of the tBLM thickness. The effect of Au_{144}TCG on the reduction of Cd^{2+} ions through the DOPC monolayer presents new evidence in favor of some molecular organization of the TCG chains inside the monolayer itself. From the viewpoint of possible applications of these modified Au_{144} MPCs, for example, as drug-delivery systems, we thus expect clusters of the Au_{144}OctA type to be quite versatile. The fact that Au_{144}TCG gets anchored to the membrane surface could be exploited to mediate ET reactions or to decorate membranes with, e.g., fluorophores.

ASSOCIATED CONTENT

Ⓢ Supporting Information

Full experimental details on methods, chemicals, syntheses, electrochemistry, and figures concerning ^{1}H NMR, TGA, UV-vis, FT-IR, and further electrochemical curves. This material is available free of charge via the Internet at http://pubs.acs.org.

AUTHOR INFORMATION

Corresponding Authors
*E-mail: lucia.becucci@unifi.it.
*E-mail: flavio.maran@unipd.it.
Notes
The authors declare no competing financial interest.

ACKNOWLEDGMENTS

REFERENCES

(1) Murray, R. W. Nanoelectrochemistry: Metal Nanoparticles, Nanoelectrodes, and Nanopores. *Chem. Rev.* **2008**, *108*, 2688−2720.

(2) Tsukuda, T. Toward an Atomic-Level Understanding of Size-Specific Properties of Protected and Stabilized Gold Clusters. *Bull. Chem. Soc. Jpn.* **2012**, *85*, 151−168.

(3) Saha, K.; Agasti, S. S.; Kim, C.; Li, X.; Rotello, V. M. Gold Nanoparticles in Chemical and Biological Sensing. *Chem. Rev.* **2012**, *112*, 2739−2779.

(4) Cho, E. C.; Xie, J.; Wurm, P.A.; Xia, Y. Understanding the Role of Surface Charges in Cellular Adsorption versus Internalization by Selectively Removing Gold Nanoparticles on the Cell Surface with I2/KI Etchant. *Nano Lett.* **2009**, *9*, 1080−1084.

(5) Ojea-Jiménez, I.; García-Fernández, L.; Lorenzo, J.; Puntes, V. F. Facile Preparation of Cationic Gold Nanoparticle-Bioconjugates for Cell Penetration and Nuclear Targeting. *ACS Nano* **2012**, *6*, 7692−7702.

(6) Lund, T.; Callaghan, M. F.; Williams, P.; Turmaine, M.; Bachmann, C.; Rademacher, T.; Roitt, I. M.; Bayford, R. The Influence of Ligand Organization on the Rate of Uptake of Gold Nanoparticles by Colorectal Cancer Cells. *Biomaterials* **2011**, *32*, 9776−9784.

(7) Chithrani, B. D.; Ghazani, A. A.; Chan, W. C. W. Determining the Size and Shape Dependence of Gold Nanoparticles Uptake into Mammalian Cells. *Nano Lett.* **2006**, *6*, 662−668.

(8) Cai, X.; Chen, H.-H.; Wang, C.-L.; Chen, S.-T.; Lai, S.-F.; Chien, C.-C.; Chen, Y.-Y.; Kempson, I. M.; Hwu, Y.; Yang, C. S.;

Margaritondo, G. Imaging the Cellular Uptake of Tiopronine-modified Gold Nanoparticles. *Anal. Bioanal. Chem.* **2011**, *401*, 809−816.

(9) Huang, K.; Ma, H.; Liu, J.; Huo, S.; Kumar, A.; Wei, T.; Zhang, X.; Jin, S.; Gan, Y.; Wang, P. C.; He, S.; Zhang, X.; Liang, X.-J. Size-Dependent Localization and Penetration of Ultrasmall Gold Nanoparticles in Cancer Cells, Multicellular Spheroids, and Tumors in Vivo. *ACS Nano* **2012**, *6*, 4483−4493.

(10) Sousa, A. A.; Morgan, J. T.; Brown, P. H.; Adams, A.; Jayasekara, M. P. S.; Zhang, G.; Ackerson, C. J.; Kruhlak, M. J.; Leapman, R. D. Synthesis, Characterization, and Direct Intracellular Imaging of Ultrasmall and Uniform Glutathione-Coated Gold Nanoparticles. *Small* **2012**, *8*, 2277−2286.

(11) Donkers, R. L.; Song, Y.; Murray, R. W. Substituent Effects on the Exchange Dynamics of Ligands on 1.6 nm Diameter Gold Nanoparticles. *Langmuir* **2004**, *20*, 4703−4707.

(12) Holm, A. H.; Ceccato, M.; Donkers, R. L.; Fabris, L.; Pace, G.; Maran, F. Effect of Peptide Ligand Dipole Moments on the Redox Potentials of Au$_{38}$ and Au$_{140}$ Nanoparticles. *Langmuir* **2006**, *22*, 10584−10589.

(13) Donkers, R. L.; Lee, D.; Murray, R. W. Synthesis and Isolation of the Molecule-like Cluster Au$_{38}$(PhCH$_2$CH$_2$S)$_{24}$. *Langmuir* **2004**, *20*, 1945−1952.

(14) Verma, A.; Uzun, O.; Hu, Y.; Hu, Y.; Han, H.-S.; Watson, N.; Chen, S.; Irvine, D. J.; Stellacci, F. Surface-structure-regulated Cell-membrane Penetration by Monolayer-protected Nanoparticles. *Nat. Mater.* **2008**, *7*, 588−595.

(15) Dekiwadia, C. D.; Lawrie, A. C.; Fecondo, J. V. Peptide Mediated Cell Penetration and Targeted Delivery of Gold Nanoparticles into Lysosomes. *J. Pept. Sci.* **2012**, *18*, 527−534.

(16) Huang, X.; El-Sayed, I. H.; Quian, W.; El-Sayed, M. A. Cancer Cell Imaging and Photothermal Therapy in the Near-Infrared Region by Using Gold Nanorods. *J. Am. Chem. Soc.* **2006**, *128*, 2115−2120.

(17) Ba, H.; Rodríguez-Fernández, J.; Stefani, F. D.; Feldmann, J. Immobilization of Gold Nanoparticles on Living Cell Membranes upon Controlled Lipid Binding. *Nano Lett.* **2010**, *10*, 3006−3012.

(18) Banerji, S. K.; Hayes, M. A. Examination of Nonendocytotic Bulk Transport of Nanoparticles across Phospholipid Membranes. *Langmuir* **2007**, *23*, 3305−3313.

(19) Urban, A. S.; Pfeiffer, T.; Fedoruk, M.; Lutich, A. A.; Feldmann, J. Single-step Injection of Gold Nanoparticles through Phospholipid Membranes. *ACS Nano* **2011**, *5*, 3585−3590.

(20) Hartono, D.; Qin, W. J.; Yang, K.-L.; Yung, L.-Y. L. Imaging the Disruption of Phospholipid Monolayer by Protein-coated Nanoparticles using Ordering Transition of Liquid Crystals. *Biomaterials* **2009**, *30*, 843−849.

(21) Leroueil, P. R.; Berry, S. A.; Duthie, K.; Han, G.; Rotello, V. M.; McNerny, D. Q.; Baker, J. R., Jr.; Orr, B. G.; Banaszak Holl, M. M. Wide Varieties of Cationic Nanoparticles Induce Defects in Supported Lipid Bilayers. *Nano Lett.* **2008**, *8*, 420−424.

(22) Park, S.-H.; Oh, S.-G.; Mun, J.-Y.; Han, S.-S. Loading of Gold Nanoparticles inside DPPC Bilayers of Liposome and their Effects on Membrane Fluidity. *Colloids Surf., B* **2006**, *48*, 112−118.

(23) Rasch, M. R.; Rossinyol, E.; Hueso, J. L.; Goodfellow, B. W.; Arbiol, J.; Korgel, B. A. Hydrophobic Gold Nanoparticle Self-assembly with Phosphatidylcholine Lipid: Membrane-loaded and Janus Vesicles. *Nano Lett.* **2010**, *10*, 3733−3739.

(24) Lin, J.; Zhang, H.; Chen, Z.; Zheng, Y. Penetration of Lipid Membranes by Gold Nanoparticles: Insights into Cellular Uptake, Cytotoxicity, and their Relationship. *ACS Nano* **2010**, *4*, 5421−5429.

(25) Qian, H.; Jin, R. Controlling Nanoparticles with Atomic Precision: The Case of Au$_{144}$(SCH$_2$CH$_2$Ph)$_{60}$. *Nano Lett.* **2009**, *9*, 4083−4087.

(26) Auvin-Guette, C.; Rebuffat, S.; Prigent, Y.; Bodo, B.; Trichogin, A. IV, an 11-Residue Lipopeptaibol from *Trichoderma Longibrachiatum*. *J. Am. Chem. Soc.* **1992**, *114*, 2170−2174.

(27) Toniolo, C.; Crisma, M.; Formaggio, F.; Peggion, C.; Epand, R. F.; Epand, R. M. Lipopeptaibols, a Novel Family of Membrane Active, Antimicrobial Petides. *Cell. Mol. Life Sci.* **2001**, *58*, 1179−1188.

(28) Peggion, C.; Formaggio, F.; Crisma, M.; Epand, R. F.; Epand, R. M.; Toniolo, C. Trichogin: A Paradigm for Lipopeptaibols. *J. Pept. Sci.* **2003**, *9*, 679−689.

(29) Becucci, L.; Maran, F.; Guidelli, R. Probing Membrane Permeabilization by the Antibiotic Lipopeptaibol Trichogin GA IV in a Tethered Bilayer Lipid Membrane. *Biochim. Biophys. Acta* **2012**, *1818*, 1656−1662.

(30) Schiller, S. M.; Naumann, R.; Lovejoy, K.; Kunz, H.; Knoll, W. Archaea Analogue Thiolipids for Tethered Bilayer Lipid Membranes on Ultrasmooth Gold Surfaces. *Angew. Chem., Int. Ed.* **2003**, *42*, 208−211.

(31) Becucci, L.; Santucci, A.; Guidelli, R. Gramicidin Conducting Dimers in Lipid Bilayers are Stabilized by Single-file Ionic Flux along them. *J. Phys. Chem. B* **2007**, *111*, 9814−9820.

(32) Becucci, L.; Guidelli, R. Kinetics of Channel Formation in Bilayer Lipid Membranes (BLMs) and Tehered BLMs: Monazomycin and Melittin. *Langmuir* **2007**, *23*, 5601−5608.

(33) Becucci, L.; Carbone, M. V.; Biagiotti, T.; D'Amico, M.; Olivotto, M.; Guidelli, R. Incorporation of the HERG Potassium Channel in a Mercury Supported Lipid Bilayer. *J. Phys. Chem. B* **2008**, *112*, 1315−1319.

(34) Becucci, L.; Papini, M.; Muller, D.; Scaloni, A.; Veglia, G.; Guidelli, R. Probing Membrane Permeabilization by the Antimicrobial Peptide Distinctin in Mercury-supported Biomimetic Membranes. *Biochim. Biophys. Acta* **2011**, *1808*, 2745−2752.

(35) Fabris, L.; Antonello, S.; Armelao, L.; Donkers, R. L.; Polo, F.; Toniolo, C.; Maran, F. Gold Nanoclusters Protected by Conformationally Constrained Peptides. *J. Am. Chem. Soc.* **2006**, *128*, 326−336.

(36) Badia, A.; Cuccia, L.; Demers, L.; Morin, F.; Lennox, R. B. Structure and Dynamics in Alkanethiolate Monolayers Self-Assembled on Gold Nanoparticles: A DSC, FT-IR, and Deuterium NMR Study. *J. Am. Chem. Soc.* **1997**, *119*, 2682−2692.

(37) Alvarez, M. M.; Khoury, J. T.; Schaaff, T. G.; Shafigullin, M. N.; Vezmar, I.; Whetten, R. L. Optical Absorption Spectra of Nanocrystal Gold Molecules. *J. Phys. Chem. B* **1997**, *101*, 3706−3712.

(38) Lee, D.; Donkers, R. L.; Wang, G.; Harper, A. S.; Murray, R. W. Electrochemistry and Optical Absorbance and Luminescence of Molecule-like Au$_{38}$ Nanoparticles. *J. Am. Chem. Soc.* **2004**, *126*, 6193−6199.

(39) Antonello, S.; Holm, A. H.; Instuli, E.; Maran, F. Molecular Electron-Transfer Properties of Au$_{38}$ Clusters. *J. Am. Chem. Soc.* **2007**, *129*, 9836−9837.

(40) Wolfe, R. L.; Murray, R. W. Analytical Evidence for the Monolayer-Protected Cluster Au$_{225}$[(S(CH$_2$)$_5$CH$_3$)]$_{75}$. *Anal. Chem.* **2006**, *76*, 1167−1173.

(41) Bizzotto, D.; Nelson, A. Continuing Electrochemical Studies of Phospholipid Monolayers of Dioleoyl Phosphatidylcholine at the Mercury-electrolyte Interface. *Langmuir* **1998**, *14*, 6269−6273.

(42) Nelson, A.; Auffret, N.; Borlakoglu, J. Interaction of Hydrophobic Organic Compounds with Mercury Adsorbed Dioleoylphosphatidylcholine Monolayers. *Biochim. Biophys. Acta* **1990**, *1021*, 205−216.

(43) Lecompte, M.-F.; Bras, A.-C.; Dousset, N.; Portas, I.; Salvayre, R.; Ayrault-Jarrier, M. Binding Steps of Apolipoprotein A-I with Phospholipid Monolayers: Adsorption and Penetration. *Biochemistry* **1988**, *37*, 16165−16171.

(44) Smalley, J. F.; Chalfant, K.; Feldberg, S. W.; Nahir, T. M.; Bowden, E. F. An Indirect Laser-Induced Temperature Jump Determination of the Surface pKa of 11-Mercaptoundecanoic Acid Monolayers Self-Assembled on Gold. *J. Phys. Chem. B* **1999**, *103*, 1676−1685.

(45) Munakata, H.; Oyamatsu, D.; Kuwabata, S. Effects of ω-Functional Groups on pH-Dependent Reductive Desorption of Alkanethiol Self-Assembled Monolayers. *Langmuir* **2004**, *20*, 10123−10128.

(46) Nicholson, R. S.; Shain, I. Theory of Stationary Electrode Polarography. Single Scan and Cyclic Methods Applied to Reversible, Irreversible, and Kinetic Systems. *Anal. Chem.* **1964**, *36*, 706−723.

(47) Guidelli, R.; Becucci, L. Estimate of the Potential Difference across Metal/Water Interfaces and across the Lipid Bilayer Moiety of Biomimetic Membranes: an Approach. *Soft Matter* **2011**, *7*, 2195−2201.

(48) Chen, S. Nanoparticle Assemblies: "Rectified" Quantized Charging in Aqueous Media. *J. Am. Chem. Soc.* **2000**, *122*, 7420−7421.

(49) Chen, S. Chemical Manipulations of Nanoscale Electron Transfers. *J. Electroanal. Chem.* **2004**, *574*, 153−165.

(50) Deng, F.; Chen, S. Electrochemical Quartz Crystal Microbalance Studies of the Rectified Quantized Charging of Gold Nanoparticles Multilayers. *Langmuir* **2007**, *23*, 936−941.

(51) Laaksonen, T.; Ruiz, V.; Liljeroth, P.; Quinn, B. M. Quantised Charging of Monolayer-protected Nanoparticles. *Chem. Soc. Rev.* **2008**, *37*, 1836−1846.

(52) Antonello, S.; Perera, N. V.; Ruzzi, M.; Gascón, J. A.; Maran, F. Interplay of Charge State, Lability, and Magnetism in the Molecule-like $Au_{25}(SR)_{18}$ Cluster. *J. Am. Chem. Soc.* **2013**, *135*, 15585−15594.

(53) Antonello, S.; Arrigoni, G.; Dainese, T.; De Nardi, M.; Parisio, G.; Perotti, L.; René, A.; Venzo, A.; Maran, F. Electron Transfer through 3D Monolayers on Au_{25} Clusters. *ACS Nano* **2014**, *8*, 2788−2795.

(54) Kumar, S. S.; Kwak, K.; Lee, D. Amperometric Sensing Based on Glutathione Protected Au_{25} Nanoparticles and Their pH Dependent Electrocatalytic Activity. *Electroanalysis* **2011**, *23*, 2116−2124.

(55) In one-half the period of an AC voltage of amplitude a and frequency f, let us assume that eN electrons move in one direction, where N is the number density of the MPCs. The resulting current density in the given direction is therefore $eN/t = 2feN$, whereas the conductance G is $2feN/(2a/\pi) = \pi feN/a$, where $2a/\pi$ is the average value of the voltage during the half period. For $f = 10$ Hz, $a = 10$ mV, and $G = 32$ μS cm^{-2}, we calculate $N = 6.4 \times 10^{10}$ molecules cm^{-2}.

(56) Baldini, C.; Peggion, C.; Falletta, E.; Moncelli, M. R.; Guidelli, R.; Toniolo, C. A Lipid Monolayer Made Permeable to Tl(I) Ions by the Lipopeptaibol Trichogin GA IV. In *Understanding Biology Using Peptides*; Blondelle, S. E., Eds.; Springer: New York, 2006; pp 265−266.

(57) Antonello, S.; Formaggio, F.; Moretto, A.; Toniolo, C.; Maran, F. Anomalous Distance Dependence of Electron Transfer across Peptide Bridges. *J. Am. Chem. Soc.* **2003**, *125*, 2874−2875.

(58) Polo, F.; Antonello, S.; Formaggio, F.; Toniolo, C.; Maran, F. Evidence Against the Hopping Mechanism as an Important Electron Transfer Pathway for Conformationally Constrained Oligopeptides. *J. Am. Chem. Soc.* **2005**, *127*, 492−493.

(59) Teixeira, V.; Feio, M. J.; Bastos, M. Role of Lipids in the Interaction of Antimicrobial Peptides with Membranes. *Prog. Lipid Res.* **2012**, *51*, 149−177.

(60) Gallová, J.; Uhríková, D.; Islamov, A.; Kuklin, A.; Balgavy, P. Effect of Cholesterol on the Bilayer Thickness in Unilamellar Extruded DLPC and DOPC Liposomes: SANS Contrast Variation Study. *Gen. Physiol. Biophys.* **2004**, *23*, 113−128.